CrystEngComm

PAPER

View Article Online
View Journal | View Issue

Cite this: *CrystEngComm*, 2022, **24**, 5748

Assembling photoactive materials from polycyclic aromatic hydrocarbons (PAHs): room temperature phosphorescence and excimer-emission in co-crystals with 1,4-diiodotetrafluorobenzene†

Alessandra Azzali, [a] Simone d'Agostino, [a] Mattia Capacci,[a] Floriana Spinelli,[a] Barbara Ventura *[b] and Fabrizia Grepioni *[a]

Received 24th May 2022,
Accepted 14th July 2022

DOI: 10.1039/d2ce00720g

rsc.li/crystengcomm

Co-crystallization between the polycyclic aromatic hydrocarbons anthracene (A) and 9-methylanthracene (MA) with 1,4-diiodotetrafluorobenzene (I2F4) afforded three novel co-crystals, *viz.* A·$(I2F4)_2$ and an unexpectedly complex system with two distinct compositions, namely MA·I2F4 and $(MA)_4$·I2F4, which can be mechanochemically interconverted by a change in the stoichiometry of the reactive mixtures. Interestingly, all co-crystals are dual-emissive materials and exhibit different mechanisms of emission. A·$(I2F4)_2$ and MA·I2F4 fluoresce from isolated molecules, whereas the luminescence of $(MA)_4$·I2F4 is dominated by excimer emission. In all cases, phosphorescence at RT (RTP) is observed and interpreted as a direct consequence of the interactions between the iodine atoms of the I2F4 co-former and the π-electron density of the anthracene aromatic rings. Furthermore, [4 + 4] photoactivity within $(MA)_4$·I2F4 was also investigated by means of FTIR/NMR spectroscopy and PXRD. The photophysical and photochemical behaviors of all solids are discussed and rationalized based on their structural features.

Introduction

Polycyclic aromatic hydrocarbons (PAHs) are a vast class of organic compounds that are composed of two or more fused aromatic rings, sharing pairs of C-atoms.[1–3]

PAHs can be the result either of natural processes, *e.g.*, the transformation of organic sediments into fossil fuels, volcanic eruptions and natural forest fires,[4,5] or, as a significant source, from anthropogenic activities, such as partial combustion of fossil fuels in industrial processes, wood-burning, tobacco-smoking, and exhaust from vehicles.[4,6] PAHs are found everywhere, from aquatic and terrestrial systems to the atmosphere,[7] and are considered highly polluting since they persist in soil and water once released into the environment.[8–12] They also tend to accumulate in food like meat, vegetables, cereals, edible oils, and seafood[13–17] and are categorized as highly toxic, mutagenic, and carcinogenic to various forms of life, including humans.[18–22] For all these reasons their emissions and levels in the environment are being regulated by government agencies, and various remediation treatments have been proposed.[4,23–25] Since the discovery of this family of compounds, scientists have proposed new applications for these pollutants, taking advantage of peculiar features such as their remarkable and unique electrical and optical properties.[26–31] By using crystal engineering principles,[32–35] valuable applications for PAHs have been developed in recent years, ranging from optical waveguides,[36] OFET-devices,[37] and additives for improving photovoltaic cell performances,[38] to bright solids, including fluorescent,[39–43] room temperature phosphorescent[44–51] and ultralong phosphorescent materials.[52–55]

In this context, co-crystallization of luminescent molecules proved to be a powerful tool for developing new materials and achieving emission type and color fine-tuning.[48,56–61] The type of co-formers to be used in co-crystallization with PAHs is rather limited, as hydrocarbons do not possess typical hydrogen bonding groups. Suitable systems are perfluoropolyhalogenated molecules, since they can drive co-crystallization by establishing halogen bonding interactions of the type X···π with the electron density of the aromatic rings in PAH molecules.[62–68] These X···π intermolecular interactions can be seen as a particular case of directional

---

[a] *Dipartimento di Chimica "Giacomo Ciamician", Università di Bologna, Via F. Selmi, 2, 40126 Bologna, Italy. E-mail: fabrizia.grepioni@unibo.it*
[b] *Istituto ISOF-CNR, Via P. Gobetti, 101, 40219 Bologna, Italy. E-mail: barbara.ventura@isof.cnr.it*

† Electronic supplementary information (ESI) available: Powder XRD patterns, TGA traces, interaction energies, NMR spectra, photophysical measurements. CCDC 2166101–2166103. For ESI and crystallographic data in CIF or other electronic format see DOI: **https://doi.org/10.1039/d2ce00720g**

halogen bonding where the electron depleted polar regions of the polarized halogens approach the electron-rich π-orbitals of an aromatic compound. Moreover, halogen atoms in close proximity to the photoactive PAH components may also promote interesting changes in their optical properties.

Within the frame of our studies on PAH co-crystals as solid luminescent materials,[53] we report here the preparation of bright crystalline materials based on the co-crystallization of anthracene (A) and its derivative 9-methylanthracene (MA), as photoactive components, and 1,4-diiodo-tetrafluorobenzene (I2F4), as a co-former (Chart 1).

New applications for these pollutants are actively being sought and are of paramount importance, especially if PAHs can be turned into valuable materials through green synthetic methods. To this end, in our co-crystallization experiments we reacted A and MA with I2F4 directly in the solid state, *via* mechanochemistry, testing different stoichiometric ratios of the pure components. Three novel co-crystals, $A{\cdot}(I2F4)_2$, MA·I2F4, and $(MA)_4{\cdot}I2F4$, have been obtained and characterized *via* a combination of X-ray diffraction (XRD) techniques and solid-state luminescence spectroscopy, the latter highlighting different optical features among the co-crystals and between the co-crystals and the pure aromatic compounds. Single crystals analysis was essential to rationalize the structure–property relationship for these solids. All co-crystals are dual-emissive materials: in A·(I2F4)2 and MA·I2F4 both fluorescence and phosphorescence from isolated A or MA molecules are observed, whereas emission from $(MA)_4{\cdot}I2F4$ is characterized by concomitant fluorescence from MA excimers and phosphorescence from the isolated molecules. Crystalline $(MA)_4{\cdot}I2F4$ is also photoactive, and its [4 + 4] photocycloaddition reaction was observed by means of FTIR spectroscopy. Finally, the stoichiometry mediated solid-state interconversion between MA·I2F4 and $(MA)_4{\cdot}I2F4$ was detected and investigated.

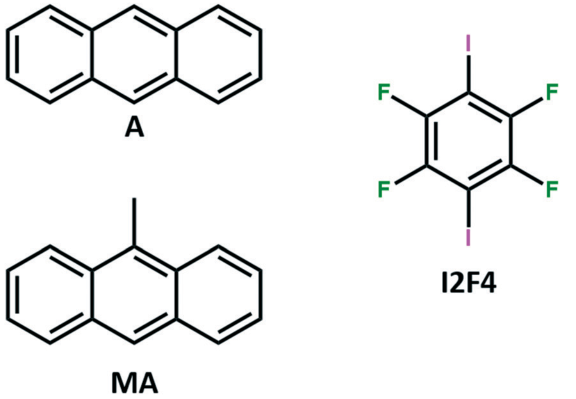

Chart 1 Molecular structure of the building blocks used in this work: the polycyclic aromatic hydrocarbons, namely, anthracene (A) and 9-methylanthracene (MA), and the co-former 1,4-diiodotetrafluorobenzene (I2F4).

Experimental

Materials

All reactants were purchased from Sigma-Aldrich and used after purification. Two PAHs, namely, anthracene (A) and 9-methylanthracene (MA), and a co-former, 1,4-diiodotetrafluorobenzene (I2F4), were recrystallized from ethanol. All solid materials were preliminarily screened for chemical and crystallographic purity *via* powder XRD analyses (see Fig. ESI-2†) and identified as anthracene form I (ANTCEN),[69] 9-methylanthracene (MANTHR01),[70] and 1,4-diiodotetrafluorobenzene form I (ZZZAVM02).[71] Reagent grade solvents were used without further purification.

Synthesis

For co-crystals $A{\cdot}(I2F4)_2$, MA·I2F4, and $(MA)_4{\cdot}I2F4$, the co-former I2F4 and the two polycyclic aromatic hydrocarbons, A or MA, were weighed in different stoichiometric ratios for a total of *ca.* 200 mg (see Table ESI-1†), transferred into 5 mL agate jars, each containing two 5 mm balls, and ground together for 2 h with a ball-milling apparatus operated at 15 Hz. The solid product was dissolved in $CHCl_3$:EtOH 1 : 1, transferred into a conical flask and kept in the dark. Slow evaporation at room temperature afforded diffraction quality single crystals.

Single-crystal XRD

Single crystal data for $A{\cdot}(I2F4)_2$, MA·I2F4, and $(MA)_4{\cdot}I2F4$ were collected at RT with an Oxford XCalibur S CCD diffractometer equipped with a graphite monochromator (Mo-Kα radiation, λ = 0.71073 Å). The crystals of MA·I2F4 were affected by twinning, for the best sample found and analyzed, two twin unit cells were indexed, and the reflection data were integrated with the default configuration for twinned crystals of the *CrysAlisPro* software. Subsequent structure solution and refinement were performed using the HKLF4 file containing non-overlapped reflections. The structures were solved by intrinsic phasing with SHELXT[72] and refined on F^2 by full-matrix least squares refinement with the program SHELXL,[73] implemented in the Olex2 software.[74,75] All non-hydrogen atoms were refined anisotropically, applying the rigid-body RIGU restraint.[76] HCH atoms for all compounds were added in calculated positions and refined riding on their respective carbon atoms. Data collection and refinement details are listed in Table 1 and Fig. ESI-1† for the Ortep plots. The programs Mercury[77] and Platon[78] were used for molecular graphics and packing index analysis, respectively. The magnitude of the main intermolecular interactions detected with co-crystals was evaluated with the Crystal Explorer Package and using CE-HF/3-21G (k_ele = 1.019; k_pol = 0.651; k_disp = 0.901; k_rep = 0.811) as energy model and basis set.[79–81] CCDC numbers 2166101–2166103.

Table 1 Crystal data and refinement details for crystalline A·(I2F4)$_2$, MA·I2F4, and (MA)$_4$·I2F4

	A·(I2F4)$_2$	MA·I2F4	(MA)$_4$·I2F4
Formula	$C_{26}H_{10}F_8I_4$	$C_{21}H_{12}F_4I_2$	$C_{66}H_{48}F_4I_2$
FW/g mol^{-1}	981.94	594.11	1170.84
Crystal system	Triclinic	Monoclinic	Triclinic
Space group	$P\bar{1}$	Pn	$P\bar{1}$
a/Å	5.9997(4)	15.2587(8)	8.1105(5)
b/Å	9.7209(10)	8.2100(3)	10.3429(5)
c/Å	12.2681(10)	16.2077(9)	16.2211(8)
α/°	73.604(8)	90	97.450(4)
β/°	89.751(6)	104.852(5)	103.319(5)
γ/°	81.821(7)	90	98.140(5)
Volume/Å^3	678.94(10)	1962.57(17)	1292.05(12)
Packing coefficient	0.68	0.67	0.67
ρ_{calc}/g cm^{-3}	2.402	2.011	1.505
μ/mm^{-1}	4.660	3.244	1.274
λ/Å	0.71073	0.71073	0.71073
Measd rflns	4495	9172	8611
Indep rflns	2655	5933	4551
R_1	0.0325	0.0289	0.0529
wR_2	0.0703	0.0910	0.1030

Powder XRD

For phase identification diffractograms were recorded on a PANalytical X'Pert Pro automated diffractometer equipped with an X'Celerator detector in Bragg–Brentano geometry, using Cu-Kα radiation (λ = 1.5418 Å) without a monochromator in the 2θ range between 3° and 30° (continuous scan mode, step size 0.0167°, counting time 19.685 s, Soller slit 0.04 rad, antiscatter slit 1/2, divergence slit 1/4, 40 mA × 40 kV). The program Mercury[77] was used for the calculation of the powder patterns, on the basis of single-crystal data retrieved from the Cambridge Structural Database (CSD) or collected in this work.

Thermogravimetric analysis

TGA measurements on all samples were performed with a PerkinElmer TGA7 thermogravimetric analyser, in the 30–300 °C temperature range, under an N_2 gas flow and at the heating rate of 5.00 °C min^{-1} (see ESI†).

Irradiation experiments

Single crystals and polycrystalline samples of (MA)$_4$·I2F4 were irradiated for 5 hours using a UV-LED (Led EnginLZ1-10UV00-0000) with λ = 365 nm and placed at 2 cm.

FTIR spectroscopy

Attenuated total reflectance Fourier transform IR (ATR-FTIR) spectra were obtained using a Bruker Alpha FT-IR spectrometer.

Optical spectroscopy

Room temperature measurements were performed on powder samples placed between two quartz slides. Reflectance spectra were acquired with a PerkinElmer Lambda 950 UV/vis/NIR spectrophotometer equipped with a 100 mm integrating sphere and converted into absorption spectra using the Kubelka–Munk function.[82] A thin layer of powder was used (absorbance values below 0.2) for luminescence measurements. Emission spectra were collected in the front-face mode with an Edinburgh FLS920 fluorimeter equipped with a Peltier-cooled Hamamatsu R928 PMT (280–850 nm) and corrected for the wavelength dependent phototube response. Gated emission spectra were acquired in the front-face mode with the same fluorimeter by using a time-gated spectral scanning mode and a μF920H Xenon flash lamp (pulse width <2 μs, repetition rate between 0.1 and 100 Hz) as an excitation source. As gating parameters, a delay of 0.1 ms and a gate of 0.5 ms were used. The spectra were corrected for the wavelength dependent phototube response. Excitation spectra were collected with the same fluorimeter operating in both modes. Emission quantum yields were determined in the solid state with the absolute method, according to Würth *et al.*,[83] by using a Labsphere barium sulfate-coated integrating sphere (diameter of 3 inches) placed in the same fluorimeter and elaborating the corrected emission spectra. The limit of detection is of the order of 1%.

Fluorescence and phosphorescence lifetimes were measured by using an IBH time-correlated single-photon counting (TCSPC) apparatus with a pulsed NanoLED excitation source at 368 nm for fluorescence and a SpectraLED at 370 nm for phosphorescence. Analysis of the luminescence decay profiles against time was accomplished with the Decay Analysis Software DAS6 provided by the manufacturer. The reported lifetimes are averaged values from 3–4 measurements. For A and A·(I2F4)$_2$ a time-resolved luminescence analysis has been performed with the same TCSPC apparatus, and the decay associated spectra (DAS) have been obtained by global analysis of the kinetic data by using the global fitting module of the DAS v6.5 software. The wavelength dependences of the amplitudes of the individual kinetic components were plotted as decay associated spectra. Estimated errors are 10% on lifetimes and quantum yields and 2 nm on emission and absorption peaks.

Solution NMR spectroscopy

1H- and ^{19}F-NMR spectra (Fig. ESI-8 and ESI-9†) were recorded on a Varian Mercury 400, and chemical shifts (δ) of NMR signals were expressed in parts per million (ppm) using an internal standard, TMS (δH = 0.00). $CDCl_3$ was bought from Cambridge Isotope Lab.

^{1}H-NMR (400 MHz, $CDCl_3$, TMS): (MA)$_4$·I2F4 before irradiation δ (ppm) 8.33 (s, 1H), 8.29–8.26 (d, 2H, CH), 8.00–7.98 (d, 2H, CH), 7.52–7.43 (m, 4H), 7.24 ($CDCl_3$), 3.09 (s, 3H, CH_3). (MA)$_4$·I2F4 after irradiation ^{1}H-NMR (400 MHz, $CDCl_3$, TMS): δ (ppm): 8.33 (s, 1H), 8.29–8.26 (d, 2H, CH), 8.00–7.98 (d, 2H, CH), 7.52–7.43 (m, 4H), 7.24 ($CDCl_3$), 7.13–7.11 (d, 2H, CH), 6.90–6.79 (m, 4H, CH), 3.99 (s,1H, CH), 3.09 (s, 3H, CH_3), 2.16 (s, 3H, CH_3). (MA)$_4$·I2F4 before and after irradiation ^{19}F NMR (377 MHz, $CDCl_3$) δ −116.89.

Results and discussion

Co-crystal synthesis and mechanochemical interconversion

Co-crystallization was carried out *via* ball-milling of the PHAs anthracene (A) or 9-methylanthracene (MA) with the co-former 1,4-diiodotetrafluorobenzene (I2F4) in several stoichiometric ratios (see Table ESI-1†).

For the pair A:I2F4, we identified a unique and novel crystalline form only when reacted in a 1 : 2 ratio, whereas for all the other stoichiometries tested, we detected unreacted materials. On the other hand, the system MA:I2F4 showed a more complex and interesting behavior, and two different and unique new phases were obtained only with the 1 : 1 and 4 : 1 ratios, whereas for all the other stoichiometries tested, we noticed also the concomitant presence of unreacted MA crystals.

The TGA measurements for all co-crystals (see ESI-4–ESI-6†) did not evidence any water or solvent loss.

The three solid products recrystallized from a $CHCl_3$: EtOH 1 : 1 mixture and were then analyzed *via* single-crystal XRD (see Table 1).

Structural analysis allowed the formulation of the co-crystals as A·$(I2F4)_2$, MA·I2F4, and $(MA)_4$·I2F4 (*vide infra* for structural description), while the comparison between the experimental and calculated patterns allowed the verification of the purity of the polycrystalline samples (see Fig. ESI-3†).

As the co-crystals MA·I2F4 and $(MA)_4$·I2F4 differ for the amount of MA in the unit cell, we tried to convert a polycrystalline sample of MA·I2F4 into $(MA)_4$·I2F4 and *vice versa* through mechanochemistry; pure $(MA)_4$·I2F4 was obtained by milling MA·I2F4 powders with three additional equivalents of MA. Analogously, conversion of $(MA)_4$·I2F4 into MA·I2F4 was achieved by adding three equivalents of co-former to powders of $(MA)_4$·I2F4. Scheme 1 depicts the overall process.

Structural features of A·(I2F4)2, (MA)4·I2F4 and MA·I2F4

The reaction of anthracene with I2F4 in the 1 : 2 stoichiometric ratio yields the co-crystal A·$(I2F4)_2$ (see Table 1). The I2F4 molecules are arranged in a ladder-like fashion (Fig. 1), with π-stacked pairs of I2F4 molecules inserted almost perpendicularly (angle between the planes *ca.* 81°) between the anthracene aromatic rings. This is reminiscent of the packing in solid anthracene; as it can be appreciated in Fig. 1c, a layer of I2F4 molecules takes the place of an analogous layer of anthracene molecules, depicted in orange in Fig. 1d. Intermolecular interactions of the X⋯π type[66,67] between the iodine atoms on I2F4 and the anthracene aromatic rings are also present [I⋯π = 3.465(6) − 3.588(4) Å], see Fig. 1d.

Alternation of the flat co-formers and 9-methylanthracene molecules is also evident in crystalline MA·I2F4. Fig. 2a shows the π-stacking (distance between the aromatic rings *ca.* 3.5 Å) of MA and I2F4 molecules along the crystallographic *b*-axis. As a consequence of this arrangement the crystal can also benefit from the stabilization effect of inter-layer weak X⋯π[66,67] halogen bonds, as depicted in Fig. 2b [I⋯π = 3.57(9) − 3.88(1) Å].

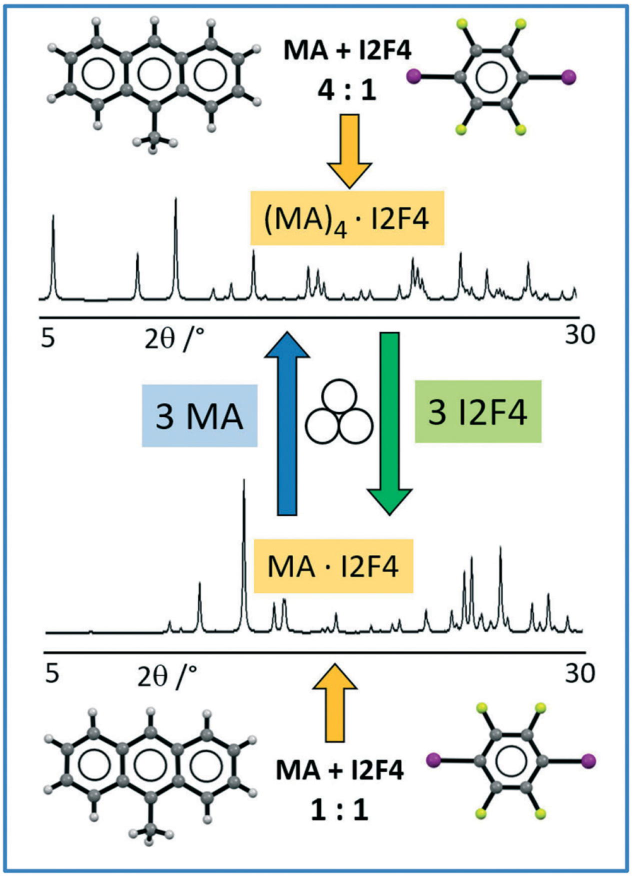

Scheme 1 Representation of mechanochemical synthesis and interconversion of crystalline $(MA)_4$·I2F4 (top) and MA·I2F4 (bottom).

If the MA:I2F4 stoichiometric ratio is increased to 4 : 1, the co-crystal $(MA)_4$·I2F4 is obtained, which presents some interesting features. The packing in this crystal can be seen to be formed from layers of the type shown in Fig. 3a. The I2F4 molecules are sandwiched (lime rectangle) between two symmetry equivalent MA molecules referred by symmetry (distance between the aromatic planes *ca.* 3.5 Å), while the

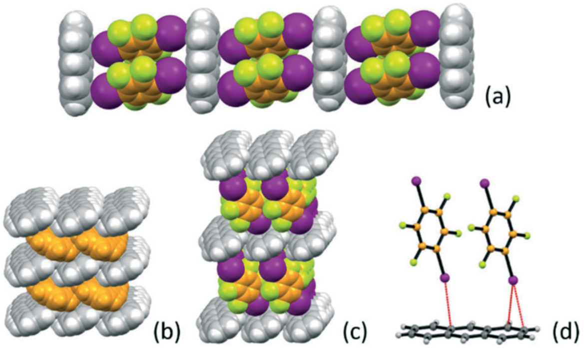

Fig. 1 (a) Space-filling representation of crystalline A·$(I2F4)_2$ showing the ladder-like alternation of anthracene and I2F4 molecules. Comparison of the layered structures in (b) solid anthracene (CSD refcode: ANTCEN) and (c) A·$(I2F4)_2$, and (d) a depiction of the X⋯π interactions at work between iodine atoms and the anthracene aromatic rings.

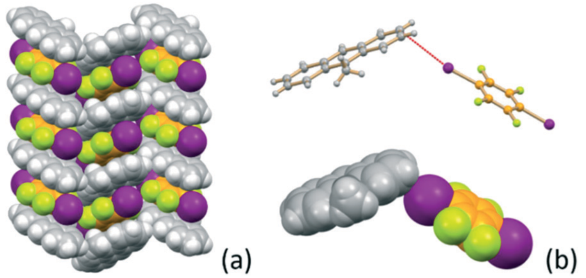

Fig. 2 (a) Columnar stacking of MA and I2F4 molecules along the *b*-axis in crystalline MA·I2F4, and (b) geometry of the X⋯π interactions at work between stackings.

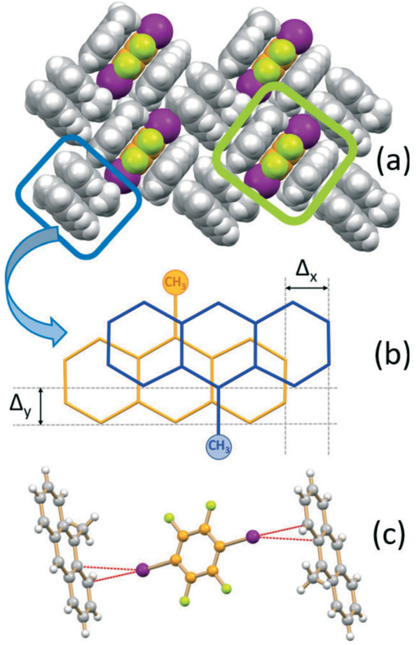

Fig. 3 Packing features of $(MA)_4$·I2F4 showing (a) the I2F4 molecules "sandwiched" between MA molecules (lime rectangle) and the π-stacked MA pairs (blue rectangle), (b) details of the head-to-tail pair arrangement (Δ*y* and Δ*x* indicate the transversal and longitudinal offsets, respectively), and (c) the geometry of the I⋯π interactions.

MA not involved in the "sandwich" are arranged in pairs (blue rectangle) and parallel and in a head-to-tail fashion, as observed in pure MA crystals;[70] this feature allows strong π–π stacking interactions, with the MA molecules at a distance of *ca.* 3.5 Å and shifted, transversally and longitudinally, by *ca.* 1.3 and 1.1 Å, respectively (Fig. 3b). The I2F4 co-former interacts laterally with these MA pairs *via* weak I⋯π halogen bonds[66,67] [I⋯π = 3.413(5), 3.413(5) Å] (see Fig. 3c).

It is worth noting that, in both A·$(I2F4)_2$ and MA·I2F4, close interaction between PAHs molecules is hindered by the presence of the I2F4 co-former, which acts as a solid "dilutant"; on the other hand, head-to-tail π-stacking of 9-methylanthracene is observed in $(MA)_4$·I2F4, analogously to what was observed in pure MA crystals.

The structural features of the compounds described above have also been examined, with the help of the program CrystalExplorer,[79–81] in terms of intermolecular interaction energies, resulting from the sum of electrostatic, polarization, dispersion and repulsion contributions. In all solids the most relevant contribution to the total potential energy comes from π-stacking arrangements, both between the I2F4 molecules, as observed in A·$(I2F4)_2$, and between MA and I2F4 or MA and MA, as can be seen for MA·I2F4 and $(MA)_4$·I2F4. I⋯π interactions also contribute in a significant manner to the total energy (see Fig. ESI-14 to ESI-16 and Tables ESI-4 to ESI-6†).

All these features play an essential role in the rationalization of the photochemical and photophysical behaviors of the three co-crystalline materials (see below).

Photoreactivity

Pairs of double bonds can behave as reactive centers and, upon irradiation, take part in a [2 + 2] or [4 + 4] solid-state photocyclization process, depending on the system under consideration. According to the topochemical postulate developed by Schmidt and coworkers in the 1960s, when the distance between the potentially reactive centers is comprised between approximately 3.6 and 4.1 Å, photocyclization, following UV irradiation, is likely to occur.[84–86] Since then, the photoreactivity of anthracene and its derivatives within molecular crystals has fascinated scientists and has been the subject of intense research over the last decades, both for theoretical purposes and potential applications.[87–95]

The arrangement of MA pairs in crystalline $(MA)_4$·I2F4 is promising from a purely geometrical point of view; therefore the possible [4 + 4] photoreactivity of the co-crystal was investigated. UV irradiation experiments on the co-crystal were first conducted on the same specimen used for single crystal XRD data collection and structural determination. Upon UV irradiation, however, the single crystals simply "crumbled". This is not surprising, as the photocyclization processes taking place within solids are almost invariably accompanied by the accumulation of stress, and when this cannot be relieved, the internal pressure may cause the single crystal to collapse and the consequent formation of amorphous or polycrystalline material.[96–98] The photoreactivity of the powder sample was also tested, and the PXRD pattern was measured after irradiation. Unfortunately, the loss of crystallinity made it impossible to identify the resulting product.

FTIR spectroscopy was therefore employed, and we could detect the presence of a photodimer within the amorphous powders. Fig. 4 shows the FTIR spectra recorded before and after irradiation. Compared to the original sample, the UV-exposed one shows a marked decrease in the band at *ca.* 885 cm^{-1}, associated with the C–H out-of-plane bending vibrations of unreacted anthracene. In contrast, the rest of the spectrum remains unaltered, thus indicating that only a fraction of MA molecules has reacted. For comparison, a pure crystalline sample of MA was also irradiated; the FTIR spectrum of the product shows the absence of the diagnostic

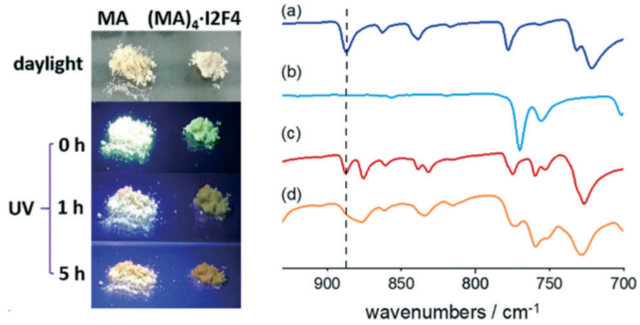

Fig. 4 Left: pictures taken during the UV irradiation of the polycrystalline samples of MA and $(MA)_4$·I2F4. Right: details of the FTIR spectra recorded on (a) crystalline MA, (b) the head-to-tail MA photodimer, (c) co-crystal $(MA)_4$·I2F4, and (d) the resulting amorphous solid after UV irradiation (right).

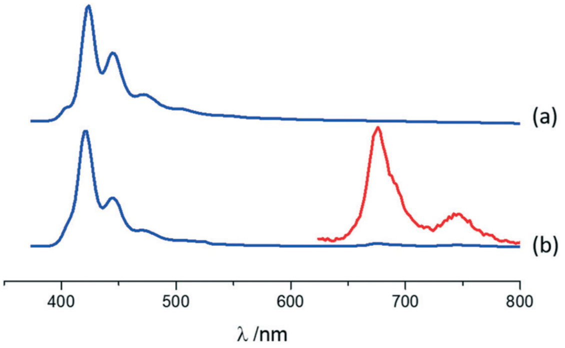

Fig. 5 Normalized luminescence spectra in the solid state for (a) pure A and (b) A·$(I2F4)_2$ (arbitrary units on the *y*-axis). λ_{exc} = 380 nm. The phosphorescence spectrum in the 650–800 nm region, isolated with a gated detection, is magnified in the inset for A·$(I2F4)_2$. The phosphorescence emission is clearly evident in A·$(I2F4)_2$ compared to solid anthracene, where no phosphorescence was detected.

band at ca 885 cm^{-1}, and the powder is then identified as a head-to-tail photodimer[99] (CSD refcode QQQFES04, see Fig. ESI-7†).

The identity of the photoproduct is also confirmed by the emergence of a new set of signals in the ^{1}H-NMR spectrum (Fig. ESI-8†), which agrees with the reported one for the head-to-tail photodimer.[100] Furthermore, ^{19}F-NMR rules out the side reactions between the polyhalogenated co-former and 9-methylanthracene (Fig. ESI-9†).

The pictures of the MA sample, taken under UV irradiation (see Fig. 4), show that, as the irradiation proceeds, the green fluorescence characteristic of this PAH vanishes with time, due to the formation of photodimers. In contrast, when crystalline $(MA)_4$·I2F4 is irradiated with UV, the color of its emission progressively changes from green to orange, likely due to the presence of unreacted MA molecules.

Luminescence spectroscopy

Photophysical features of A·$(I2F4)_2$, MA·I2F4, and $(MA)_4$·I2F4 were also investigated using solid-state absorption and luminescence spectroscopy, with the purpose of (i) characterizing the emission properties of the compounds resulting from the co-crystallization and (ii) highlighting the differences with those of parent crystalline materials, *i.e.*, anthracene (A) and 9-methylanthracene (MA).

For co-crystal A·$(I2F4)_2$, the absorption and luminescence profiles are very similar to those of pure anthracene (see ESI†). Both compounds display fluorescence with a clear vibronic structure (see Fig. 5 and Fig. ESI-10;† main maxima at 424, 446 and 472 nm for A, blue-shift of 2 nm in A·$(I2F4)_2$), as reported for anthracene crystals.[101] In A·$(I2F4)_2$, as mentioned above, the I2F4 co-former acts as a "dilutant" towards anthracene molecules, preventing the formation of strong intermolecular interactions of π-stacking or herring-bone type, and this accounts for a monomeric-type emission. The emission of the co-crystal is much weaker than that of pure A: quantum yields of 12.6% and 0.8% are measured for A and A·$(I2F4)_2$, respectively. Moreover, close inspection of the emission spectrum of A·$(I2F4)_2$ evidences the additional emission bands in the range 650–800 nm. By using a pulsed source and applying a gated detection we could assign these bands to the phosphorescence spectrum of anthracene in the co-crystal. Fig. 5 shows the isolated spectrum, with two clear vibronic bands at 676 nm and 746 nm. These results indicate that the presence of I···π interactions in the co-crystal promotes the intersystem crossing in the PAHs molecules, thus quenching fluorescence and enabling phosphorescence at RT in a completely organic material.[44,53] The excitation spectra collected in both the fluorescence and phosphorescence modes are almost superimposable (see Fig. ESI-10†).

The fluorescence lifetime analysis for A and A·$(I2F4)_2$ is reported in the ESI.†

A similar characterization technique was performed for pure MA and its co-crystals. The emission of MA is characterized by a broad band peaking at 522 nm (Fig. 6 and

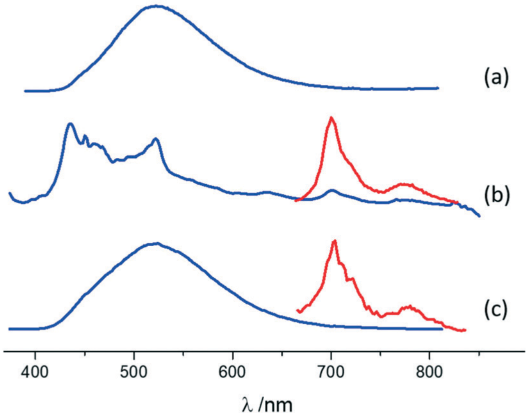

Fig. 6 Normalized luminescence spectra in the solid state of (a) pure MA, (b) MA·I2F4, and (c) $(MA)_4$·I2F4 (arbitrary units on the *y*-axis). λ_{exc} = 380 nm. The phosphorescence spectra in the 650–850 nm region, isolated with a gated detection, are magnified in the inset for MA·I2F4 and $(MA)_4$·I2F4. In both co-crystals the phosphorescence emission is clearly evidenced compared to the parent PAH 9-methylanthracene, where no phosphorescence was detected at all. Moreover, for MA·I2F4 the spectrum is not dominated by excimer emission.

ESI-11†), typical of excimer fluorescence.[102] Excimer emission in crystals of anthracene derivatives is not common and has been observed under high pressures[101,103] or in particular crystal designs.[104,105] The luminescence features of MA·I2F4 are markedly different from those of pure MA crystals: a weak and vibronically resolved fluorescence is observed, accompanied by a clear phosphorescence emission (Fig. 6 and ESI-11†). The latter spectrum, isolated by means of gated detection, shows bands at 700 nm and 774 nm. Such differences are a consequence of the two types of MA molecular arrangements. In the parent crystal, PAHs are suitably paired to produce excimer emission and photoreact.[99] On the other hand, within MA·I2F4, the MA molecules are almost isolated and at a longer distance, hindering *de-facto* the formation of excimers. The "lighting-up" of phosphorescence in the range 650–850 nm is a result of the external heavy atom effect exerted by the co-former.

Co-crystal $(MA)_4$·I2F4 still shows different luminescence properties, since both excimer fluorescence (with maximum at 522 nm) and phosphorescence (with peaks at 702 nm and 778 nm) are observed (Fig. 6 and ESI-11†). The crystal arrangement of $(MA)_4$·I2F4 features both paired and isolated MA molecules, leading to an emission pattern where the excimer contribution prevails. The presence of phosphorescence, even if weaker than in MA·I2F4, is particularly interesting in combination with excimer emission and can be ascribed to the isolated molecules interacting with the co-former.

Emission quantum yields of 9.0% and 13.4% are found for MA and $(MA)_4$·I2F4, respectively, while for MA·I2F4, a low value of *ca.* 0.1% (below experimental resolution) is measured.

The fluorescence lifetimes measured for MA and its co-crystals agree with the proposed luminescence mechanisms. A lifetime of *ca.* 6 ns is detected for MA·I2F4, where a monomeric emission prevails, and a bi-exponential decay with longer lifetimes of *ca.* 27 ns and 62 ns is observed for pure MA, indicative of excimer emission (Table ESI-2†). In the case of $(MA)_4$·I2F4, lifetimes of the order of 6 ns and 36 ns can be ascribed to the presence of both monomeric and excimer emission, even if the latter is dominant in the steady-state spectrum.

Phosphorescence lifetimes were measured for A·$(I2F4)_2$, MA·I2F4 and $(MA)_4$·I2F4. In all cases the decays could be fitted using bi-exponential functions, with lifetimes of the order of 30 μs and 200 μs for A·$(I2F4)_2$ and MA·I2F4 and longer lifetimes of *ca.* 90 μs and 320 μs for $(MA)_4$·I2F4 (Table ESI-3†). The increase of the phosphorescence lifetime in $(MA)_4$·I2F4 can be due to the lower conformer/PAH ratio of this co-crystal, which leads to a reduced heavy atom effect in promoting both intersystem crossing and the phosphorescence rate.

Conclusions

In this work, we reported the mechanochemical synthesis of the three novel co-crystals, namely, A·$(I2F4)_2$, MA·I2F4, and $(MA)_4$·I2F4, containing the polycyclic aromatic hydrocarbons, anthracene (A) or methylanthracene (MA), and the co-former 1,4-diodotetrafluorobenzene (I2F4).

The mainframe for this work was the potential re-use of pollutants as novel interesting materials. The choice of a polyhalogenated co-former was instrumental in obtaining solid-state products possessing remarkable and unprecedented luminescence features.

A peculiar aspect is that all co-crystals exhibit phosphorescence at room temperature, contrary to what observed for the parent crystalline anthracene and 9-methylanthracene, which show only fluorescence. The presence of excimer emission in (MA)4·I2F4 is also interesting, as this emission mechanism is combined with the phenomenon of phosphorescence within the same material.

The two co-crystals MA·I2F4 and $(MA)_4$·I2F4 were shown to interconvert in the solid state, *via* mechanochemistry, upon the addition of an excess of the limiting component; finally, in the case of $(MA)_4$·I2F4, containing pairs of MA molecules in a favourable relative orientation, the potential [4+4] photoreactivity was also investigated.

Work is in progress to further test the ability of polyhalogenated co-formers to direct the assembly of organic co-crystals with controllable luminescence, able to display phosphorescence at room temperature. This approach also offers the possibility to achieve photoreactive materials with intriguing photophysical properties.

Author contributions

AA, MC and FS: experimentation and data collection; AA and SD: conceptualization and manuscript preparation; SD: structural analysis and data validation; BV and FG: funding acquisition and supervision.

Conflicts of interest

The authors declare that they have no known competing financial interests or personal relationships that could have appeared to influence the work reported in this paper.

Acknowledgements

The authors acknowledge the University of Bologna (RFO-scheme), MUR, project PRIN2020 "Nature inspired crystal engineering", and CNR (Project PHEEL) for financial support.

Notes and references

1 J. C. Fetzer, *Polycyclic Aromat. Compd.*, 2007, **27**, 143–162.
2 A. T. Lawal, *Cogent Environ. Sci.*, 2017, **3**, 1339841.
3 B. R. T. Simoneit, in *PAHs and Related Compounds. The Handbook of Environmental Chemistry*, ed. A. H. Neilson, Springer, Berlin, Heidelberg, 1998, pp. 175–221.
4 H. I. Abdel-Shafy and M. S. M. Mansour, *Egypt. J. Pet.*, 2016, **25**, 107–123.

5 K. Ravindra, R. Sokhi and R. Van Grieken, *Atmos. Environ.*, 2008, **42**, 2895–2921.

6 M. Tobiszewski and J. Namieśnik, *Environ. Pollut.*, 2012, **162**, 110–119.

7 B. J. Finlayson-Pitts and J. N. Pitts, *Science*, 1997, **276**, 1045–1051.

8 K. C. Jones, J. A. Stratford, K. S. Waterhouse, E. T. Furlong, W. Giger, R. A. Hites, C. Schaffner and A. E. Johnston, *Environ. Sci. Technol.*, 1989, **23**, 95–101.

9 C.-C. Lee, C. S. Chen, Z.-X. Wang and C.-J. Tien, *Sci. Total Environ.*, 2021, **795**, 148867.

10 A. O. Adeniji, O. O. Okoh and A. I. Okoh, *Arch. Environ. Contam. Toxicol.*, 2019, **76**, 657–669.

11 A. O. Adeniji, O. O. Okoh and A. I. Okoh, in *Recent Insights in Petroleum Science and Engineering*, ed. M. Zoveidavianpoor, IntechOpen, Rijeka, 2018, pp. 393–428.

12 A. Turaki Usman, H. O. Abugu and C. O. B. Okoye, *J. Environ. Health Sci. Eng.*, 2021, **19**, 1523–1534.

13 O. S. Olatunji, O. S. Fatoki, B. O. Opeolu and B. J. Ximba, *Food Chem.*, 2014, **156**, 296–300.

14 G. R. Sampaio, G. M. Guizellini, S. A. da Silva, A. P. de Almeida, A. C. C. Pinaffi-Langley, M. M. Rogero, A. C. de Camargo and E. A. F. S. Torres, *Int. J. Mol. Sci.*, 2021, **22**, 6010.

15 R. H. de Vos, W. van Dokkum, A. Schouten and P. de Jong-Berkhout, *Food Chem. Toxicol.*, 1990, **28**, 263–268.

16 H. Ekner, K. Dreij and I. Sadiktsis, *Food Control*, 2022, **132**, 108528.

17 Y.-R. Ju, C.-F. Chen, M.-H. Wang, C.-W. Chen and C.-D. Dong, *J. Hazard. Mater.*, 2022, **421**, 126708.

18 R. Stading, G. Gastelum, C. Chu, W. Jiang and B. Moorthy, *Semin. Cancer Biol.*, 2021, **76**, 3–16.

19 C. Torres-Moreno, L. Puente-DelaCruz, G. Codling, A. L. Villa, M. Cobo, J. Klanova and B. Johnson-Restrepo, *Environ. Res.*, 2022, **204**, 111981.

20 Z. Nováková, J. Novák, M. Bittner, P. Čupr, P. Přibylová, P. Kukučka, M. Smutná, B. I. Escher, H. Demirtepe, A. Miralles-Marco and K. Hilscherová, *J. Hazard. Mater.*, 2022, **424**, 127306.

21 L. Zhang, H. Wang, Z. Yang, B. Fang, H. Zeng, C. Meng, S. Rong and Q. Wang, *Environ. Pollut.*, 2022, **293**, 118493.

22 R. Tong, L. Cao, X. Yang and B. Zhang, *Int. Arch. Occup. Environ. Health*, 2021, **94**, 1917–1929.

23 C. E. Cerniglia, *Curr. Opin. Biotechnol.*, 1993, **4**, 331–338.

24 A. B. Patel, S. Shaikh, K. R. Jain, C. Desai and D. Madamwar, *Front. Microbiol.*, 2020, **11**, 1–23.

25 L. N. Ukiwe, U. U. Egereonu, P. C. Njoku, C. I. A. Nwoko and J. I. Allinor, *Int. J. Chem.*, 2013, **5**, 43–55.

26 P. Yu, Y. Li, H. Zhao, L. Zhu, Y. Wang, W. Xu, Y. Zhen, X. Wang, H. Dong, D. Zhu and W. Hu, *Small*, 2021, **17**, 2006574.

27 L. H. Nguyen and T. N. Truong, *ACS Omega*, 2018, **3**, 8913–8922.

28 C. Aumaitre and J.-F. Morin, *Chem. Rec.*, 2019, **19**, 1142–1154.

29 G. Malloci, G. Cappellini, G. Mulas and A. Mattoni, *Chem. Phys.*, 2011, **384**, 19–27.

30 I. Cherchneff, J. R. Barker and A. G. G. M. Tielens, *Astrophys. J.*, 1991, **377**, 541.

31 G. M. Paternò, Goudappagouda, Q. Chen, G. Lanzani, F. Scotognella and A. Narita, *Adv. Opt. Mater.*, 2021, **9**, 2100508.

32 D. Braga, F. Grepioni, L. Maini and S. D'Agostino, *IUCrJ*, 2017, **4**, 369–379.

33 D. Braga, F. Grepioni, L. Maini and S. d'Agostino, *Eur. J. Inorg. Chem.*, 2018, **2018**, 3597–3605.

34 G. R. Desiraju, *J. Am. Chem. Soc.*, 2013, **135**, 9952–9967.

35 C. B. Aakeröy and K. R. Seddon, *Chem. Soc. Rev.*, 1993, **22**, 397–407.

36 D. Tian and Y. Chen, *Adv. Opt. Mater.*, 2021, **9**, 2002264.

37 B. L. Hu and Q. Zhang, *Chem. Rec.*, 2021, **21**, 116–132.

38 J. Lee, J. Shim, J. S. Lee, C.-J. Choi, S.-Y. Yim, Y. Jin, K. Yu, Y. J. Park, S. Ahn and D. I. Son, *J. Mater. Chem. C*, 2021, **9**, 13081–13089.

39 R. M. Hochstrasser and A. Malliaris, *Mol. Cryst. Liq. Cryst.*, 1970, **11**, 331–342.

40 Y. Ishii and A. Matsui, *J. Phys. Soc. Jpn.*, 1967, **22**, 926.

41 H.-D. Wu, H.-D. Peng and G.-B. Pan, *RSC Adv.*, 2016, **6**, 78979–78983.

42 R. M. Hochstrasser, *J. Chem. Phys.*, 1962, **36**, 1099–1100.

43 H. Wu, M. Li, C. Sun, X. Wang and Z. Su, *Dalton Trans.*, 2020, **49**, 5087–5091.

44 S. d'Agostino, F. Grepioni, D. Braga and B. Ventura, *Cryst. Growth Des.*, 2015, **15**, 2039–2045.

45 L. Li, Z. F. Liu, W. X. Wu and W. J. Jin, *Acta Crystallogr., Sect. B: Struct. Sci., Cryst. Eng. Mater.*, 2018, **74**, 610–617.

46 M. Villa, S. D'Agostino, P. Sabatino, R. Noel, J. Busto, M. Roy, M. Gingras and P. Ceroni, *New J. Chem.*, 2020, **44**, 3249–3254.

47 B. Ventura, A. Bertocco, D. Braga, L. Catalano, S. d'Agostino, F. Grepioni and P. Taddei, *J. Phys. Chem. C*, 2014, **118**, 18646–18658.

48 M. Singh, K. Liu, S. Qu, H. Ma, H. Shi, Z. An and W. Huang, *Adv. Opt. Mater.*, 2021, **9**, 1–24.

49 D. Li, F. Lu, J. Wang, W. Hu, X.-M. Cao, X. Ma and H. Tian, *J. Am. Chem. Soc.*, 2018, **140**, 1916–1923.

50 J. Yang, X. Zhen, B. Wang, X. Gao, Z. Ren, J. Wang, Y. Xie, J. Li, Q. Peng, K. Pu and Z. Li, *Nat. Commun.*, 2018, **9**, 1–10.

51 Y. Xie, Y. Ge, Q. Peng, C. Li, Q. Li and Z. Li, *Adv. Mater.*, 2017, **29**, 1606829.

52 X.-N. Li, M. Yang, X.-L. Chen, J.-H. Jia, W.-W. Zhao, X.-Y. Wu, S.-S. Wang, L. Meng and C.-Z. Lu, *Small*, 2019, **15**, 1903270.

53 S. D'Agostino, F. Spinelli, P. Taddei, B. Ventura and F. Grepioni, *Cryst. Growth Des.*, 2019, **19**, 336–346.

54 R. Kabe and C. Adachi, *Nature*, 2017, **550**, 384–387.

55 S. Xu, R. Chen, C. Zheng and W. Huang, *Adv. Mater.*, 2016, **28**, 9920–9940.

56 J. C. Christopherson, F. Topić, C. J. Barrett and T. Friščić, *Cryst. Growth Des.*, 2018, **18**, 1245–1259.

57 F. Grepioni, S. D'Agostino, D. Braga, A. Bertocco, L. Catalano and B. Ventura, *J. Mater. Chem. C*, 2015, **3**, 9425–9434.

58 B. Lu, X. Fang and D. Yan, *ACS Appl. Mater. Interfaces*, 2020, **12**, 31940–31951.
59 X. G. Yang, W. J. Qin, J. R. Zhang, X. K. Tian, X. Fan, L. F. Ma and D. Yan, *Front. Chem.*, 2021, **9**, 851.
60 Q. Feng, W. Huan, J. Wang, F. Guo, J. Lu, G. Diao and Y. Shan, *Crystals*, 2018, **8**, 392.
61 W. Ji, B. Xue, S. Bera, S. Guerin, Y. Liu, H. Yuan, Q. Li, C. Yuan, L. J. W. Shimon, Q. Ma, E. Kiely, S. A. M. Tofail, M. Si, X. Yan, Y. Cao, W. Wang, R. Yang, D. Thompson, J. Li and E. Gazit, *ACS Nano*, 2020, **14**, 10704–10715.
62 V. Kumar, P. Scilabra, P. Politzer, G. Terraneo, A. Daolio, F. Fernandez-Palacio, J. S. Murray and G. Resnati, *Cryst. Growth Des.*, 2021, **21**, 642–652.
63 G. Cavallo, P. Metrangolo, R. Milani, T. Pilati, A. Priimagi, G. Resnati and G. Terraneo, *Chem. Rev.*, 2016, **116**, 2478–2601.
64 A. Priimagi, G. Cavallo, P. Metrangolo and G. Resnati, *Acc. Chem. Res.*, 2013, **46**, 2686–2695.
65 C. B. Aakeröy, M. Baldrighi, J. Desper, P. Metrangolo and G. Resnati, *Chem. – Eur. J.*, 2013, **19**, 16240–16247.
66 L. Li, W. X. Wu, Z. F. Liu and W. J. Jin, *New J. Chem.*, 2018, **42**, 10633–10641.
67 X. Pang, H. Wang, W. Wang and W. J. Jin, *Cryst. Growth Des.*, 2015, **15**, 4938–4945.
68 M. Arhangelskis, F. Topić, P. Hindle, R. Tran, A. J. Morris, D. Cinčić and T. Friščić, *Chem. Commun.*, 2020, **56**, 8293–8296.
69 R. Mason, *Acta Crystallogr.*, 1964, **17**, 547–555.
70 J. C. J. Bart and G. M. J. Schmidt, *Isr. J. Chem.*, 1971, **9**, 429–448.
71 S. Y. Oh, C. W. Nickels, F. Garcia, W. Jones and T. Friščić, *CrystEngComm*, 2012, **14**, 6110–6114.
72 G. M. Sheldrick, *Acta Crystallogr., Sect. A: Found. Adv.*, 2015, **71**, 3–8.
73 G. M. Sheldrick, *Acta Crystallogr., Sect. C: Struct. Chem.*, 2015, **71**, 3–8.
74 O. V. Dolomanov, L. J. Bourhis, R. J. Gildea, J. A. K. Howard and H. Puschmann, *J. Appl. Crystallogr.*, 2009, **42**, 339–341.
75 A. A. Sarjeant, 2015, 1–50.
76 A. Thorn, B. Dittrich and G. M. Sheldrick, *Acta Crystallogr., Sect. A: Found. Crystallogr.*, 2012, **68**, 448–451.
77 C. F. Macrae, P. R. Edgington, P. McCabe, E. Pidcock, G. P. Shields, R. Taylor, M. Towler and J. van de Streek, *J. Appl. Crystallogr.*, 2006, **39**, 453–457.
78 A. L. Spek, *J. Appl. Crystallogr.*, 2003, **36**, 7–13.
79 P. R. Spackman, M. J. Turner, J. J. McKinnon, S. K. Wolff, D. J. Grimwood, D. Jayatilaka and M. A. Spackman, *J. Appl. Crystallogr.*, 2021, **54**, 1006–1011.
80 C. F. Mackenzie, P. R. Spackman, D. Jayatilaka and M. A. Spackman, *IUCrJ*, 2017, **4**, 575–587.
81 S. P. Thomas, P. R. Spackman, D. Jayatilaka and M. A. Spackman, *J. Chem. Theory Comput.*, 2018, **14**, 1614–1623.
82 K. Rurack and M. Spieles, *Anal. Chem.*, 2011, **83**, 1232–1242.
83 C. Würth, M. Grabolle, J. Pauli, M. Spieles and U. Resch-Genger, *Nat. Protoc.*, 2013, **8**, 1535–1550.
84 G. M. J. Schmidt, *J. Chem. Soc.*, 1964, 385.
85 M. D. Cohen, G. M. J. Schmidt and F. I. Sonntag, *J. Chem. Soc.*, 1964, 2000–2013.
86 E. Heller and G. M. J. Schmidt, *Isr. J. Chem.*, 1971, **9**, 449–462.
87 T. Salzillo, I. Bilotti, R. G. Della Valle, E. Venuti and A. Brillante, *J. Am. Chem. Soc.*, 2012, **134**, 17671–17679.
88 T. Salzillo, E. Venuti, C. Femoni, R. G. Della Valle, R. Tarroni and A. Brillante, *Cryst. Growth Des.*, 2017, **17**, 3361–3370.
89 L. Opilik, P. Payamyar, J. Szczerbiński, A. P. Schütz, M. Servalli, T. Hungerland, A. D. Schlüter and R. Zenobi, *ACS Nano*, 2015, **9**, 4252–4259.
90 F. Spinelli, S. d'Agostino, P. Taddei, C. D. Jones, J. W. Steed and F. Grepioni, *Dalton Trans.*, 2018, **47**, 5725–5733.
91 T. Salzillo, S. Zaccheroni, R. G. Della Valle, E. Venuti and A. Brillante, *J. Phys. Chem. C*, 2014, **118**, 9628–9635.
92 T. Salzillo, E. Venuti, R. G. Della Valle and A. Brillante, *J. Raman Spectrosc.*, 2017, **48**, 271–277.
93 T. Salzillo and A. Brillante, *CrystEngComm*, 2019, **21**, 3127–3136.
94 G. Hofer, A. D. Schlüter and T. Weber, *Macromolecules*, 2022, **55**, 568–583.
95 T. Kim, L. Zhu, L. J. Mueller and C. J. Bardeen, *J. Am. Chem. Soc.*, 2014, **136**, 6617–6625.
96 D. Braga, S. d'Agostino and F. Grepioni, *Cryst. Growth Des.*, 2012, **12**, 4880–4889.
97 G. Kaupp, J. Schmeyers, M. Kato, K. Tanaka and F. Toda, *J. Phys. Org. Chem.*, 2002, **15**, 148–153.
98 D. Bučar, T. D. Hamilton and L. R. MacGillivray, in *Organic Nanostructures*, ed. J. L. Atwood and J. W. Steed, Wiley-VCH Verlag GmbH & Co. KGaA, Weinheim, Germany, 2008, pp. 305–311.
99 A. F. Mabied, M. Müller, R. E. Dinnebier, S. Nozawa, M. Hoshino, A. Tomita, T. Sato and S. Adachi, *Acta Crystallogr., Sect. B: Struct. Sci.*, 2012, **68**, 424–430.
100 D. Y. Wu, B. Chen, X. G. Fu, L. Z. Wu, L. P. Zhang and C. H. Tung, *Org. Lett.*, 2003, **5**, 1075–1077.
101 Z. A. Dreger, H. Lucas and Y. M. Gupta, *J. Phys. Chem. B*, 2003, **107**, 9268–9274.
102 J. B. Birks and J. B. Aladekomo, *Photochem. Photobiol.*, 1963, **2**, 415–418.
103 Y. Dai, H. Liu, T. Geng, F. Ke, S. Niu, K. Wang, Y. Qi, B. Zou, B. Yang, W. L. Mao and Y. Lin, *J. Mater. Chem. C*, 2021, **9**, 934–938.
104 H. Liu, D. Cong, B. Li, L. Ye, Y. Ge, X. Tang, Y. Shen, Y. Wen, J. Wang, C. Zhou and B. Yang, *Cryst. Growth Des.*, 2017, **17**, 2945–2949.
105 Y. Mizobe, M. Miyata, I. Hisaki, Y. Hasegawa and N. Tohnai, *Org. Lett.*, 2006, **8**, 4295–4298.